Supporting Information

Achieving low dielectric constant and high thermal conductivity polymer composites by using larger POSS functionalized boron nitride nanosheets

Ming-Xi Nie, Jian Wang, Qin Zhang*, Di Han*, and Qiang Fu

College of Polymer Science & Engineering, State Key Laboratory of Polymer Materials

Engineering, Sichuan University, Chengdu 610065, P. R. China

* Corresponding authors. E-mail: handi@scu.edu.cn (D. H.), qinzhang@scu.edu.cn (Q. Z.)

1. Experimental Section

Preparation of hydroxylated boron nitride nanosheets (BN-OH). The title material was prepared by exfoliating commercial *h*-BN through hydroxide-assisted ball milling using a vertical planetary ball mill.[1] The specific operation was as follows: *h*-BN (2 g) and NaOH aqueous solution (2 M) were added into a zirconia ball mill jar with zirconia balls at ball-to-powder ratio of 50:1, and the mixture underwent milling at 500 rpm for 24 h. Subsequently, the ball-milled mixture was centrifuged at 3000 rpm for 30 min to remove unexfoliated bulk boron nitride. The resulting solid was washed three times with HCl (0.1 M) solution and deionized water to eliminate residual NaOH. After drying in a vacuum oven at 70 °C for 24 h, BN-OH was obtained as a white powder. Yield: 20%.

Instrumentation and Characterizations. ^{1}H NMR spectra were acquired in CDCl$_3$ using a Bruker 400 MHz NMR spectrometer at room temperature. Fourier transform infrared (FT-IR) spectra were recorded on a Nicolet 6700 spectrometer in attenuated total reflection model and ransmission

mode. Thermo gravimetric analysis (TGA) was tested on a TA Q500 thermo-analyzer from room temperature to 600 °C at a heating rate of 10 °C min^{-1} under nitrogen condition. Thermal mechanical analyzer (TMA) was measured on a TA Q400EM instrument using tension mode with a pre-stress of 0.01 N and a heating rate of 5 °C min^{-1}. The atomic force microscope (AFM) images of surface morphology were measured on a Dimension Icon (Bruker, America) in Tapping mode in a 20 μm × 20 μm area. Scanning electron microscope (SEM) images were recorded on a Nova NanoSEM 450 field emission SEM. The accelerating voltage was 15 kV and all samples were sputter-coated with a thin layer of gold before characterization. Transmission electron microscope (TEM) images were recorded on a Thermo Scientific Talos F200i TEM instrument with an accelerating voltage of 80 kV. Water contact Angle (WCA) was measured with a Kruss DSA25 instrument at ambient temperature. The water drop volume in each test was 2 μL, and the WCA value was calculated from three measurements. Wide-angle X-ray diffraction (WAXD) was performed on a Rigaku Ultima IV X-ray diffractometer with a Cu Kα radiation (40 kV and 40 mA) and in the diffraction angle (2θ) range from 2 to 60°. X-ray photoelectron spectroscopy (XPS) spectra were performed on an Axis Ultra DLD, UK with an Al Kα radiation (15 kV) to analyze functionalization and element content of filler. The dielectric constant and dielectric loss of samples were tested using a Novocontrol Concept 50 broad frequency dielectric spectrometer with a frequency ranging from 1 Hz to 1 MHz. Dynamic mechanical analysis (DMA) was performed on a TA Q800 instrument from 40 to 250 °C with the ramp temperature of 5 °C min^{-1} and the frequency of 1 Hz, and sample dimension used for each test was 30 mm × 5 mm × 1 mm. Tensile properties were determined on Instron 5966 instrument at room temperature with a strain rate of 10 mm min^{-1}. Density was measured on MatsuHaku MH-120E density tester at room temperature. Before measurement, the upper and lower surfaces of the samples were coated with a thin layer of gold to ensure the contact between the copper electrodes and the samples. The thermal conductivity

(T_C) of composite materials were calculated according to the equation: $T_C = \alpha * \rho * C$, where α, ρ and C respectively correspond to thermal diffusivity, density $(g \cdot cm^{-3})$ and specific heat capacity $(J \cdot kg^{-1} \cdot K^{-1})$. The test samples were thin films with a diameter of around 25 mm and a thickness of approximately 300 μm. Thermal diffusivity in both horizontal and vertical directions was measured using different test molds. Measurements were conducted at 25 °C using a thermal diffusivity analyzer (LFA467, NETZSCH), with an average of 5 data points per measurement. C values of PDCPD, BN-T_8N, BN-T_{10}N, and BN-T_{12}N were respectively measured by differential scanning calorimetry (DSC, TA) using sapphire as the standard. Meanwhile, the specific heat capacity of the composite material was calculated according to the equation: $C = \varphi C_{BN-T_nN} + (1 - \varphi)C_{PDCPD}$, where φ, C_{BN-T_nN} and C_{PDCPD} respectively correspond to the weight fractions (wt%) of POSS modified fillers (BN-T), the specific heat capacity of the POSS modified fillers (BN-T), and the specific heat capacity of PDCPD. Sample water absorption was calculated according to the following equation:

$$WA\ (\%) = \frac{m - m_0}{m_0} \times 100$$

where m_0 was the constant weight of the fully crosslinked sample after drying at 80°C for 1 day, and m was the weight of the samples immersed in deionized water for different times. Positron annihilation lifetime spectrum (PALS) was detected using an automated fast-slow coincidence system with a channel width of 6.16 ps and a time resolution of 250 ps. Two identical disk-like samples, measuring 15 mm in diameter and 1.0 mm in thickness, were sandwiched around a 2×10^5 Bq ^{22}Na positron source wrapped in aluminum foil. Approximately 2.5×10^6 counts were collected at room temperature for each test, and the data were analyzed using LT 9.0 software. The temperature distribution images of different samples were recorded using an infrared thermal imager (FLIR-T600). To evaluate the thermal management capability, the samples were coated with graphite to ensure similar surface optical properties, and then placed on a 90 °C hot stage.

2. Supplementary Schemes and Characterization Data

Scheme S1. Synthetic routes of T_8VS, $T_{10}VS$, and $T_{12}VS$.[a]
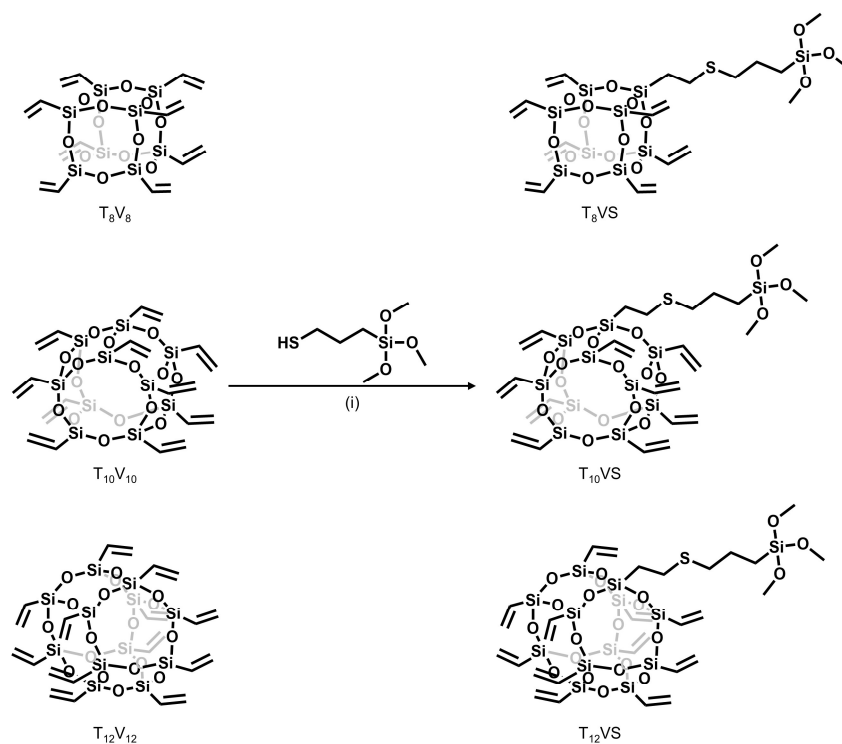
[a] Reagent and conditions: (i) DMPA, THF, R.T., UV (365nm), 15 min, yield: ~32% for T_8VS, ~28% for $T_{10}VS$, and ~31% for $T_{12}VS$. The existence of multi-functionalized products should be noted in addition to the mono-functionalized product.
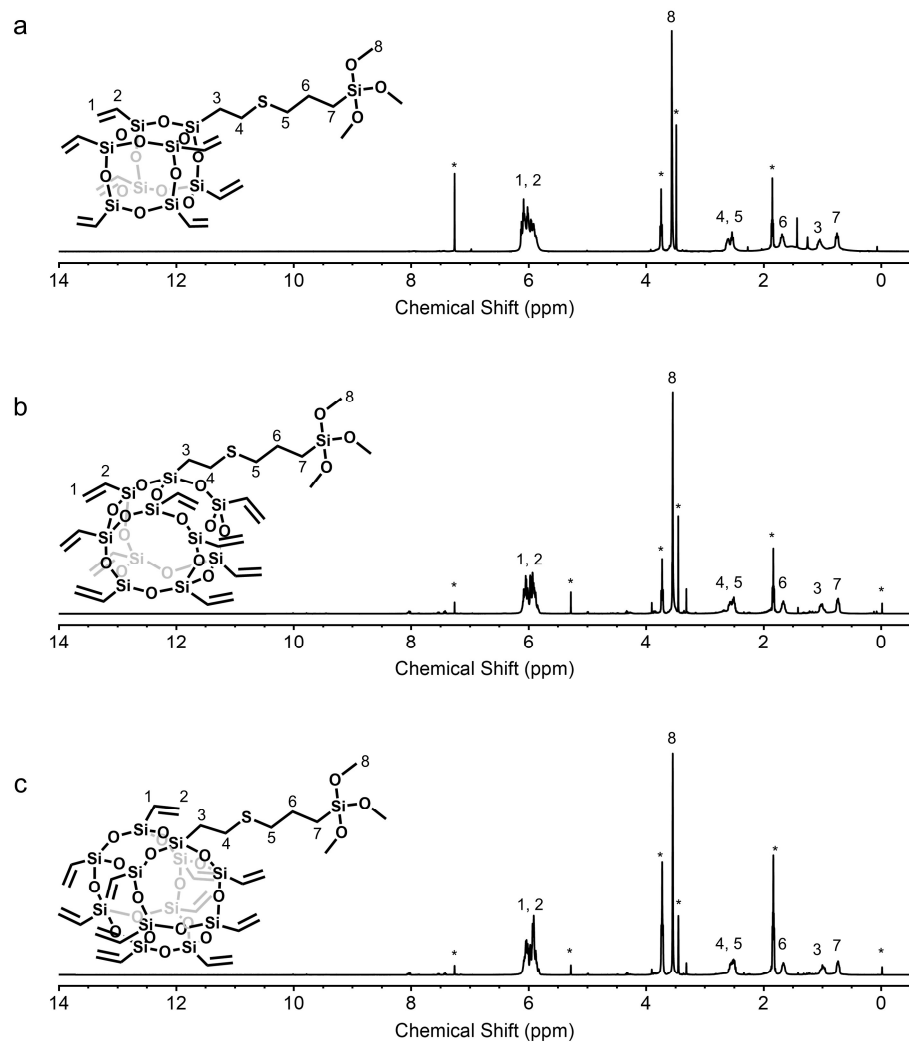
Figure S1. ^{1}H NMR of (a) T_8VS, (b) $T_{10}VS$, and (c) $T_{12}VS$. Asterisk represents signal from $CDCl_3$, THF, methanol, and TMS.

5
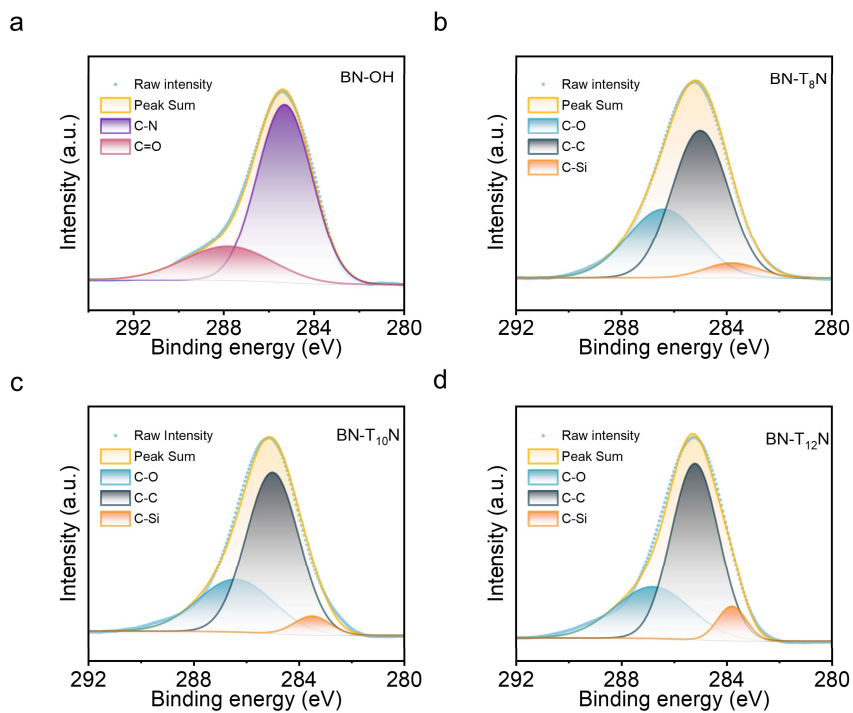
Figure S2. XPS C1s peak-splitting results of (a) BN-OH, (b) BN-T$_8$N, (c) BN-T$_{10}$N, and (d) BN-T$_{12}$N.
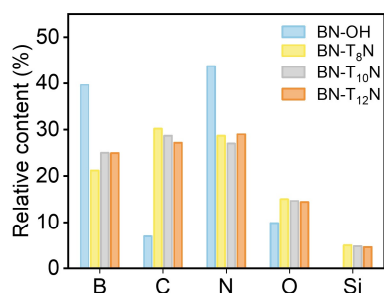
Figure S3. Atomic percentage (%) of BN-OH, BN-T$_8$N, BN-T$_{10}$N and BN-T$_{12}$N obtained by XPS analysis.
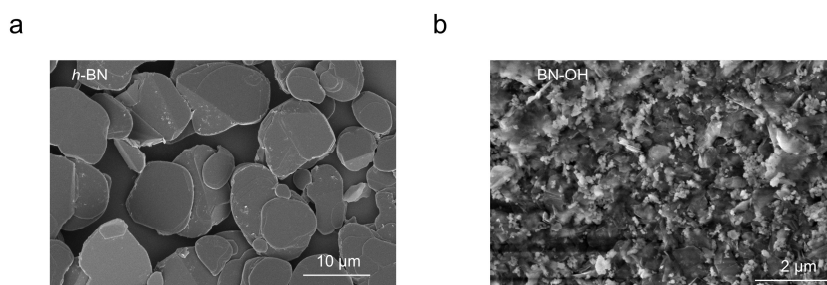
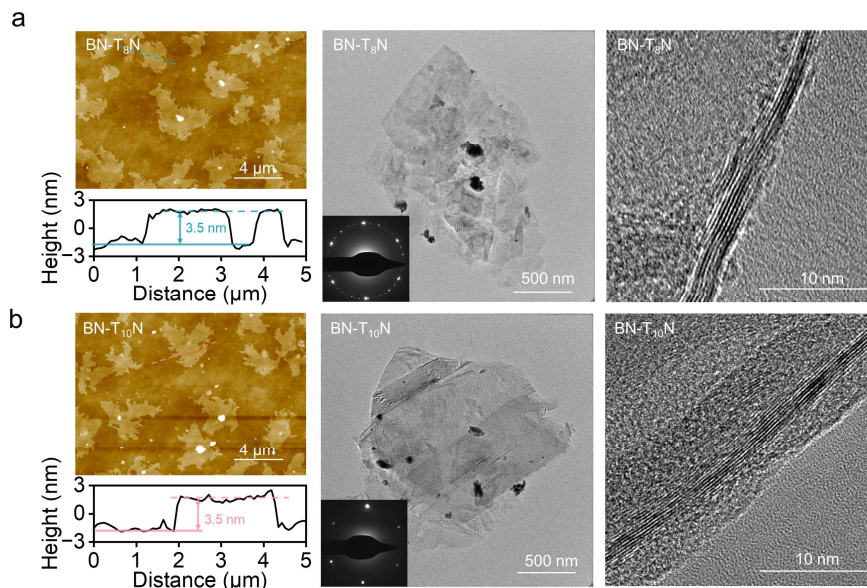**Figure S4.** SEM images of (a) *h*-BN and (b) BN-OH.

Figure S5. AFM height images, TEM images, HRTEM, and SAED images of (a) BN-T$_8$N and (b) BN-T$_{10}$N.
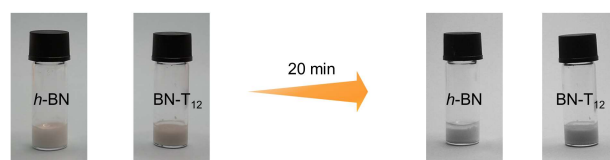

Figure S6. Images of DCPD monomer with 15 wt% of *h*-BN, and BN-T$_{12}$N, respectively, indicating the good dispersion and stability of BN-T$_{12}$N in DCPD.
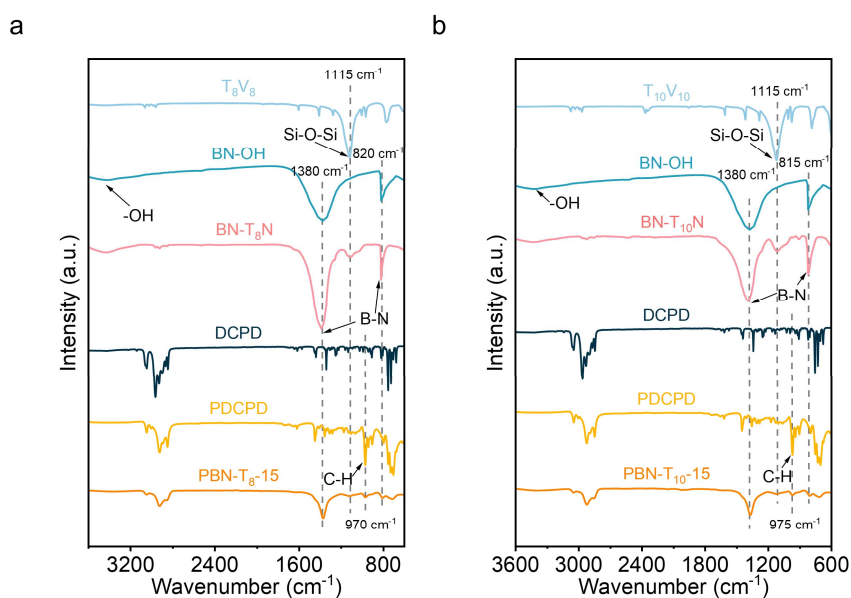

Figure S7. FT-IR spectra of (a) T$_8$V$_8$, BN-OH, BN-T$_8$N, DCPD, PDCPD, and PBN-T$_8$-15; (b) T$_{10}$V$_{10}$, BN-OH, BN-T$_{10}$N, DCPD, PDCPD and PBN-T$_{10}$-15 nanocomposites.
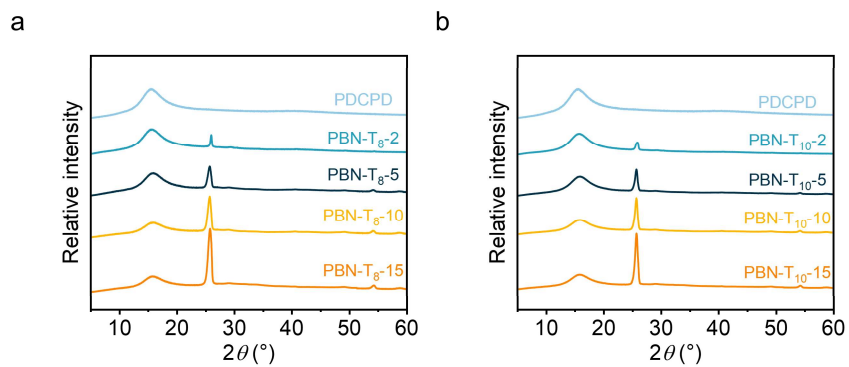
Figure S8. WAXD patterns of (a) PBN-T_8 and (b) PBN-T_{10} nanocomposites.
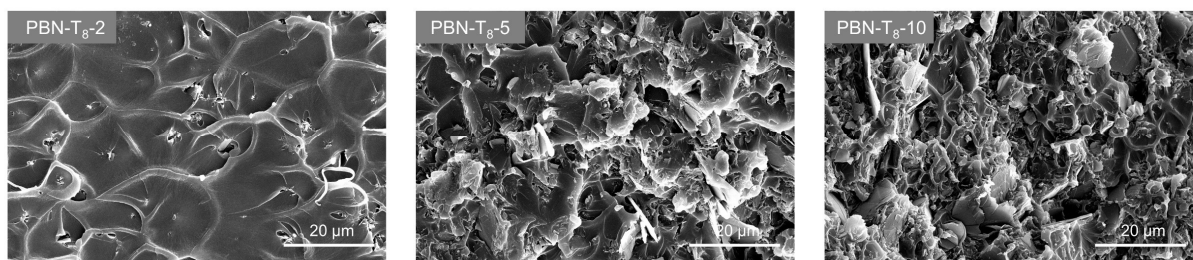

Figure S9. SEM images of PBN-T_8-2, PBN-T_8-5, and PBN-T_8-10 nanocomposites.
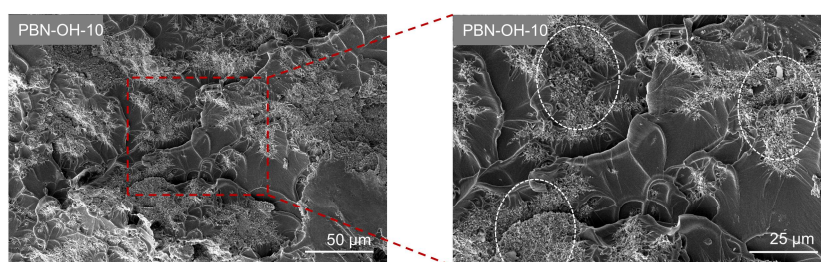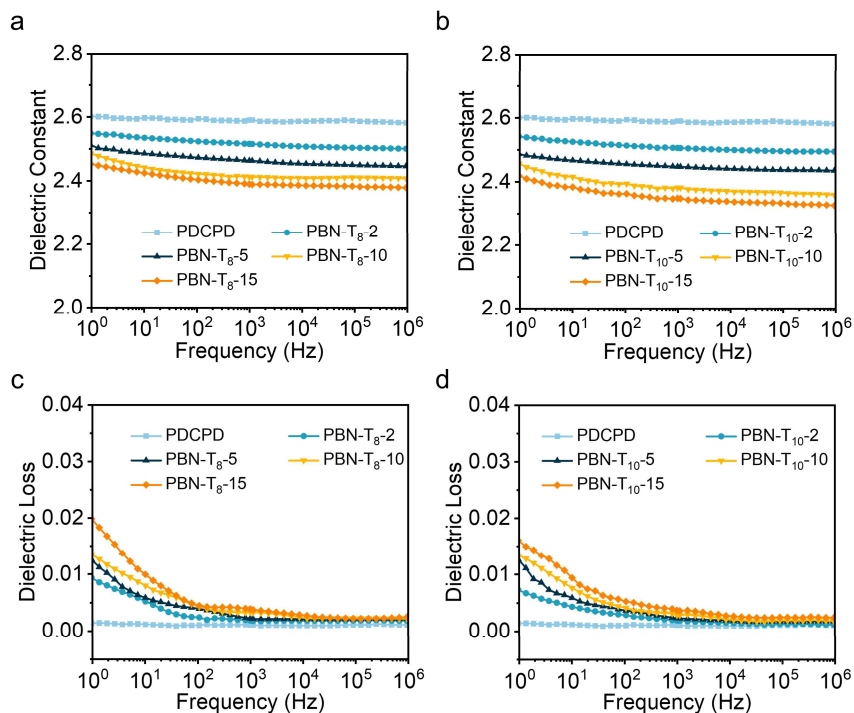

Figure S10. SEM images of PBN-OH-10.

Figure S11. Dielectric constant and dielectric loss of (a, c) PDCPD and PBN-T$_8$ with varying BN-T$_8$N content, and (b, d) PDCPD and PBN-T$_{10}$N with varying BN-T$_{10}$ content versus frequency at ambient temperature, where the frequency ranges from 1 to 10^6 Hz.
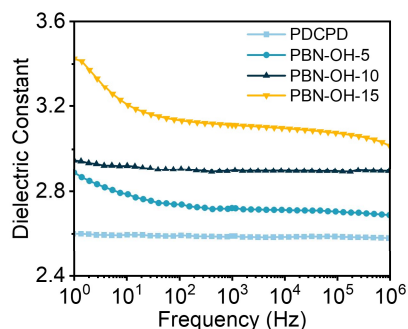

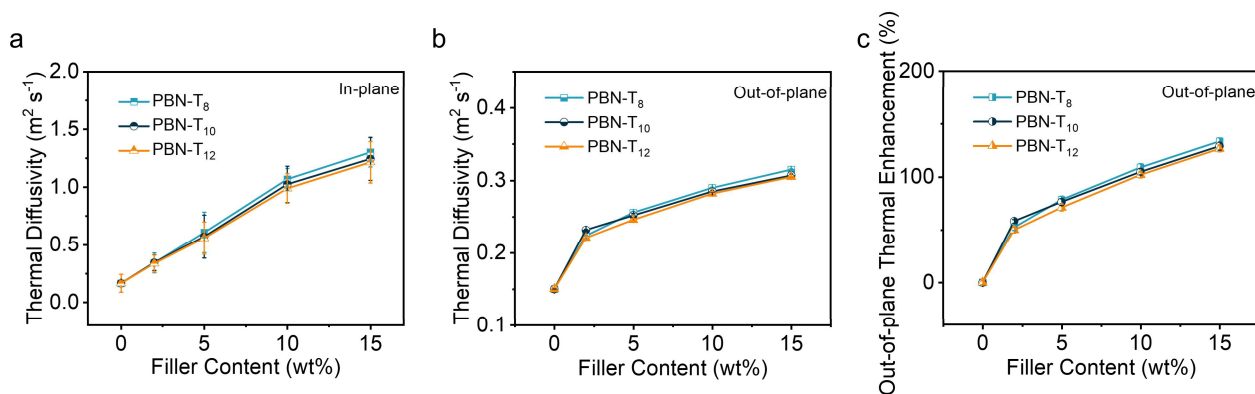**Figure S12**. Dielectric constant of PBN-OH with varying BN-OH content versus frequency at room temperature.

Figure S13. (a) In-plane thermal diffusivity, (b) out-of-plane thermal diffusivity, and (c) out-of-plane thermal conductivity enhancement of PBN-T$_8$, PBN-T$_{10}$ and PBN-T$_{12}$ nanocomposites.
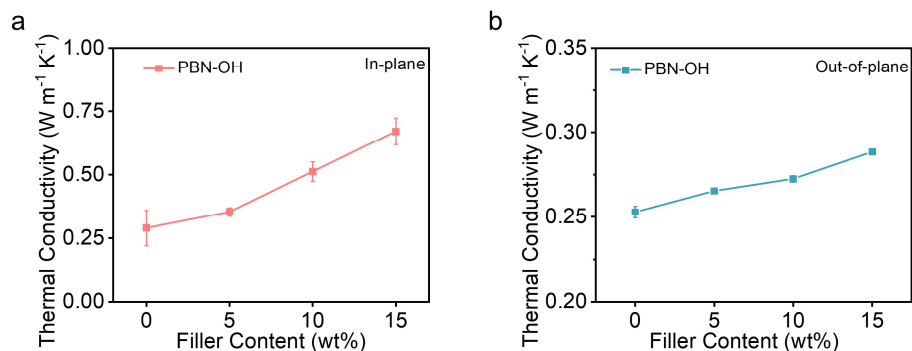
Figure S14. (a) In-plane thermal conductivity, and (b) out-of-plane thermal conductivity of PBN-OH with 0, 5, 10, and 15 wt% of BN-OH.
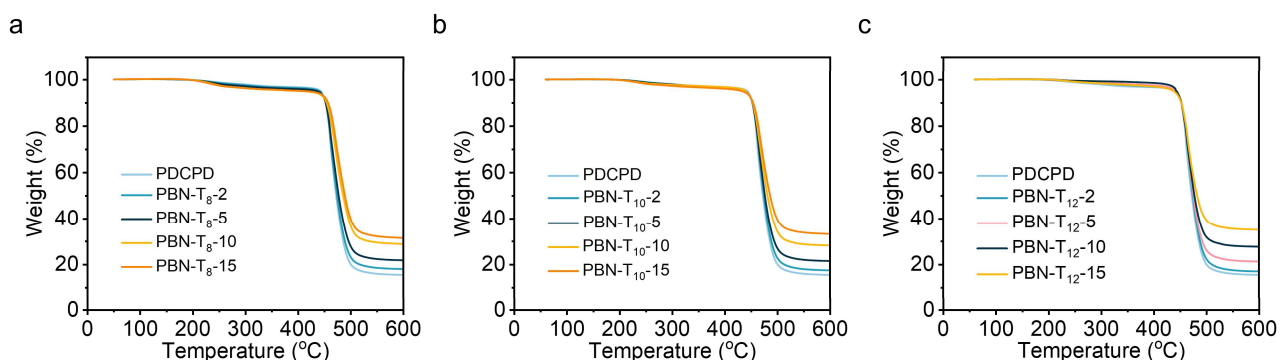
Figure S15. TGA curves of (a) PBN-T$_8$, (b) PBN-T$_{10}$, and (c) PBN-T$_{12}$ with varying BN-T$_n$N content under nitrogen atmosphere.
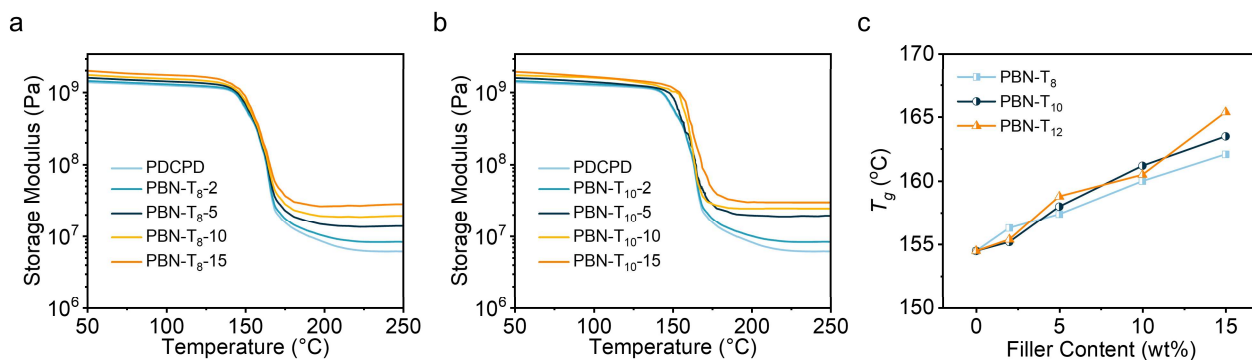
Figure S16. Representative storage modulus of (a) PDCPD and PBN-T$_8$, (b) PDCPD and PBN-T$_{10}$ with varying BN-T$_n$N content. (c) T_g of PBN-T$_8$, PBN-T$_{10}$, and PBN-T$_{12}$ with varying BN-T$_n$N content obtained from DMA testing.

Figure S17. Tan δ of (a) PDCPD and PBN-T$_8$, and (b) PDCPD and PBN-T$_{10}$ versus temperature.
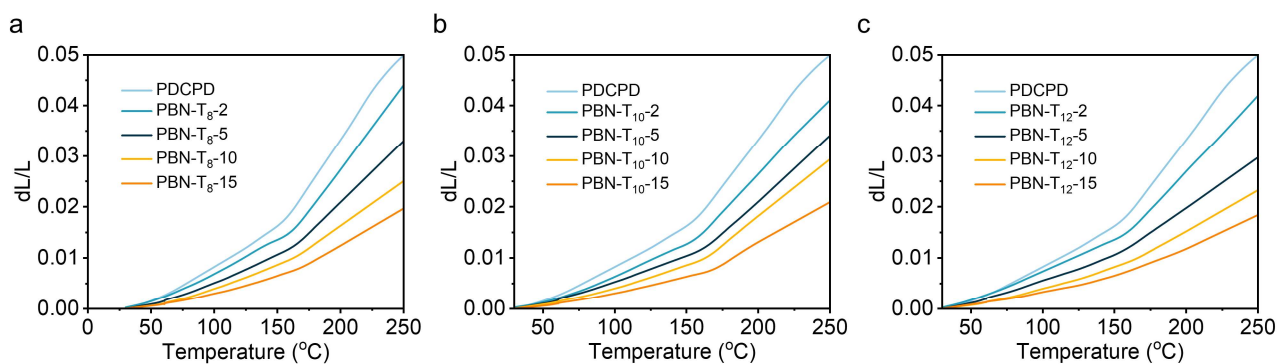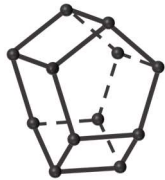
Figure S18. TMA curves of PDCPD, (a) PBN-T$_8$, (b) PBN-T$_{10}$, and (c) PBN-T$_{12}$ with different BN-T$_n$N content.

Table S1. Information on T_8, T_{10}, and T_{12} POSS cage sizes.

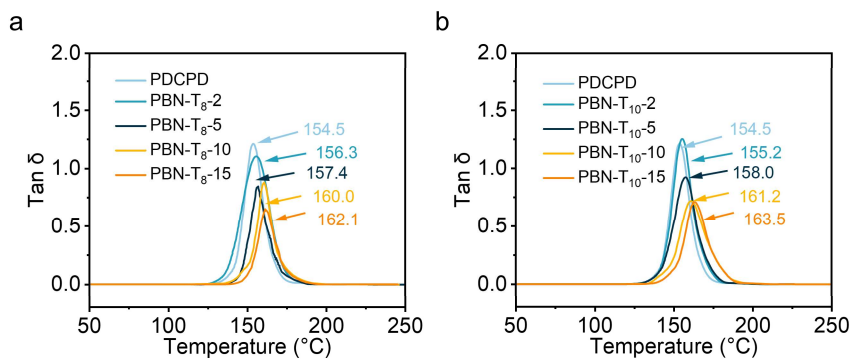|	T_8	T_{10}	T_{12}
POSS Cage [a]			
l (Å) [b]	3.117	3.128	3.151
V (Å^3)	l^3	$\dfrac{5\tan 54°}{4} l^3$	$\left(\dfrac{\sqrt{3}+5\tan 54°}{4}\right) l^3$
	30.3	52.6	67.4

[a] The structure of T_8, T_{10}, and T_{12} POSS cages are acquired from literatures and can be simplified as polyhedrons.[2-5] [b] The Si-O-Si bond lengths of T_8, T_{10}, and T_{12} POSS were acquired from reported results.

Table S2. Atomic percentage (%) obtained by XPS analysis of h-BN, BN-OH, BN-T$_8$N, BN-T$_{10}$N, and BN-T$_{12}$N.

Sample	B (%)	C (%)	N (%)	O (%)	Si (%)
h-BN	38.24	14.61	41.38	5.77	0
BN-OH	39.61	6.89	43.69	9.83	0
BN-T$_8$	21.18	30.18	28.67	14.99	4.98
BN-T$_{10}$	24.98	28.65	26.97	14.63	4.77
BN-T$_{12}$	24.94	27.12	28.97	14.38	4.58

Table S3. Specific heat capacity of PDCPD, BN-T$_8$N, BN-T$_{10}$N, and BN-T$_{12}$N nanocomposites.

Sample	Specific heat capacity (J g^{-1} K^{-1}, 25 ºC)
PDCPD	1.57
BN-T$_8$	0.93
BN-T$_{10}$	0.95
BN-T$_{12}$	0.95

Table S4. Volume fraction, density, and specific heat capacity of PDCPD, PBN-T$_8$, PBN-T$_{10}$, PBN-T$_{12}$, nanocomposites.

	Mass fraction (wt%)	Volume fraction (vol%)	Density [a] (g cm^{-3})	Specific heat capacity [b] (J g^{-1} K^{-1}, 25 °C)
PDCPD	0.00	0.00	1.028 ± 0.003	1.57
PBN-T$_8$-2	2.00	0.84	1.056 ± 0.007	1.56
PBN-T$_8$-5	5.00	2.13	1.096 ± 0.008	1.54
PBN-T$_8$-10	10.00	4.38	1.155 ± 0.009	1.51
PBN-T$_8$-15	15.00	6.79	1.221 ± 0.008	1.47
PBN-T$_{10}$-2	2.00	0.82	1.059 ± 0.004	1.56
PBN-T$_{10}$-5	5.00	2.08	1.101 ± 0.006	1.54
PBN-T$_{10}$-10	10.00	4.29	1.152 ± 0.007	1.51
PBN-T$_{10}$-15	15.00	6.65	1.220 ± 0.008	1.48
PBN-T$_{12}$-2	2.00	0.86	1.053 ± 0.006	1.56
PBN-T$_{12}$-5	5.00	2.19	1.094 ± 0.007	1.54
PBN-T$_{12}$-10	10.00	4.52	1.148 ± 0.005	1.51
PBN-T$_{12}$-15	15.00	7.00	1.215 ± 0.007	1.48

[a] Determined by density meter. [b] Determined by DSC and Calculated by the formula: $C_{composites} = C_1 \times \varphi_1 + C_2 \times (1 - \varphi_1)$,[6] where $C_{composites}$, C_1, C_2, and φ_1 respectively represent the specific heat capacity of the composite material, the specific heat capacity of the filler, the specific heat capacity of the polymer, and the mass fraction of the filler.

Table S5. 5% weight loss temperature (T_{d5}), 10% weight loss temperature (T_{d10}), and residual weight (R_w) of PBN-T$_8$, PBN-T$_{10}$ and PBN-T$_{12}$ nanocomposites.

Materials	T_{d5} (°C)	T_{d10} (°C)	R_w (%)
PDCPD	443.2	452.5	15.5
PBN-T$_8$-2	440.9	452.4	18.0
PBN-T$_8$-5	436.3	452.5	21.8
PBN-T$_8$-10	408.8	454.1	28.9
PBN-T$_8$-15	413.9	457.0	31.6
PBN-T$_{10}$-2	439.9	452.5	17.5
PBN-T$_{10}$-5	440.2	452.6	21.5
PBN-T$_{10}$-10	440.4	453.0	28.3
PBN-T$_{10}$-15	433.2	454.0	33.3
PBN-T$_{12}$-2	439.3	452.8	17.0
PBN-T$_{12}$-5	441.8	452.7	21.3
PBN-T$_{12}$-10	443.4	452.5	27.7
PBN-T$_{12}$-15	438.2	452.2	35.2

References

1. D. Lee, B. Lee, K. H. Park, H. J. Ryu, S. Jeon and S. H. Hong, *Nano Lett.*, 2015, **15**, 1238-1244.

2. P. A. Agaskar and W. G. Klemperer, *Inorg. Chim. Acta*, 1995, **229**, 355-364.

3. M. Laird, A. Van der Lee, D. G. Dumitrescu, C. Carcel, A. Ouali, J. R. Bartlett, M. Unno and M. Wong Chi Man, *Organometallics*, 2020, **39**, 1896-1906.

4. M. Laird, N. Herrmann, N. Ramsahye, C. Totée, C. Carcel, M. Unno, J. R. Bartlett and M. Wong Chi Man, *Angew. Chem. Int. Ed.*, 2021, **60**, 3022-3027.

5. D.-L. Zhou, J.-H. Li, Q.-Y. Guo, X. Lin, Q. Zhang, F. Chen, D. Han and Q. Fu, *Adv. Funct. Mater.*, 2021, **31**, 2102074.

6. Y. Zhang, C. Lei, K. Wu and Q. Fu, *Adv. Sci.*, 2021, **8**, 2004821.